Gas-Phase Synthesis of Trimetallic Nanoparticles

Jean-Gabriel Mattei,[†] Panagiotis Grammatikopoulos,*[,†] Junlei Zhao,[‡] Vidyadhar Singh,[†] Jerome Vernieres,[†] Stephan Steinhauer,[†] Alexander Porkovich,[†] Eric Danielson,[†] Kai Nordlund,[‡] Flyura Djurabekova,[‡] and Mukhles Sowwan*[,†]

[†]Nanoparticles by Design Unit, Okinawa Institute of Science and Technology (OIST) Graduate University, 1919-1 Tancha, Onna-Son, Okinawa 904-0495, Japan

[‡]Department of Physics and Helsinki Institute of Physics, University of Helsinki, P.O. Box 43, FI-00014 Helsinki, Finland

S *Supporting Information*

ABSTRACT: To this day, engineering nanoalloys beyond bimetallic compositions has scarcely been within the scope of physical deposition methods due to the complex, nonequilibrium processes they entail. Here, we report a gas-phase synthesis strategy for the growth of multimetallic nanoparticles: magnetron-sputtering inert-gas condensation from neighboring monoelemental targets provides the necessary compositional flexibility, whereas in-depth atomistic computer simulations elucidate the fast kinetics of nucleation and growth that determines the resultant structures. We fabricated consistently trimetallic Au−Pt−Pd nanoparticles, a system of major importance for heterogeneous catalysis applications. Using high-resolution transmission electron microscopy, we established their physical and chemical ordering: Au/Pt-rich core@Pd-shell atomic arrangements were identified for particles containing substantial amounts of all elements. Decomposing the growth process into basic steps by molecular dynamics simulations, we identified a fundamental difference between Au/Pt and Pd growth dynamics: Au/Pt electronic arrangements favor the formation of dimer nuclei instead of larger-size clusters, thus significantly slowing down their growth rate. Consequently, larger Pd particles formed considerably faster and incorporated small Au and Pt clusters by means of in-flight decoration and coalescence. A broad range of icosahedral, truncated-octahedral, and spheroidal face-centered cubic trimetallic nanoparticles were reproduced in simulations, in good agreement with experimental particles. Comparing them with their expected equilibrium structures obtained by Monte Carlo simulations, we identified the particles as metastable, due to out-of-equilibrium growth conditions. We aspire that our in-depth study will constitute a significant advance toward establishing gas-phase aggregation as a standard method for the fabrication of complex nanoparticles by design.
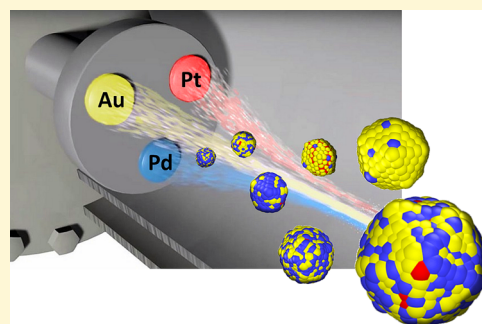
INTRODUCTION

Gas-phase synthesis is a promising method for the green and economic design of nanoparticles as building blocks for targeted nanotechnology applications, which has attracted increasing interest due to its versatility and liberating independence from chemical precursors and surfactants.[1] Today, after significant advances both in the laboratory and in silico,[2−5] it has reached the liminal stage where its potential for real-world applications can be realized. To this end, two main limitations need to be overcome: scale-up and structural control.[6,7] This work has nothing to do with the former; it has, however, everything to do with the latter.

A manifestation of the technique's coming-of-age would be the consistent design and engineering of sophisticated, multicomponent nanoparticles of high technological relevance; however, to this day, the majority of reports typically concern simple mono- or bimetallic particles. The comparative advantage of multicomponent nanoparticles composed of various elements is twofold: on the one hand, they can offer multiple functionalities, combining different classes of chemical and physical properties stemming from individual constituents.

On the other hand, through coupling between different components, multielemental nanoparticles can present improved or even novel properties typically unavailable to single-element nanoparticles.[8] These advantages make multielemental nanoparticles particularly attractive for a wide range of potential applications; a common example is the use of ternary magneto-plasmonic nanoparticles for theranostics.[9,10] As a result, a large number of studies have been published over the past years demonstrating the correlation between the composition, structure, and physical or chemical properties of numerous multielemental systems.[11−14]

Of particular interest is the boost that multimetallic nanoparticles can provide to the field of catalysis. For example, Pt-based multicomponent nanoparticles have been extensively utilized in the chemical industry.[15,16] Pt presents remarkable catalytic activity, which may be further enhanced by the addition of another metallic component such as Au or Pd.[17−20]
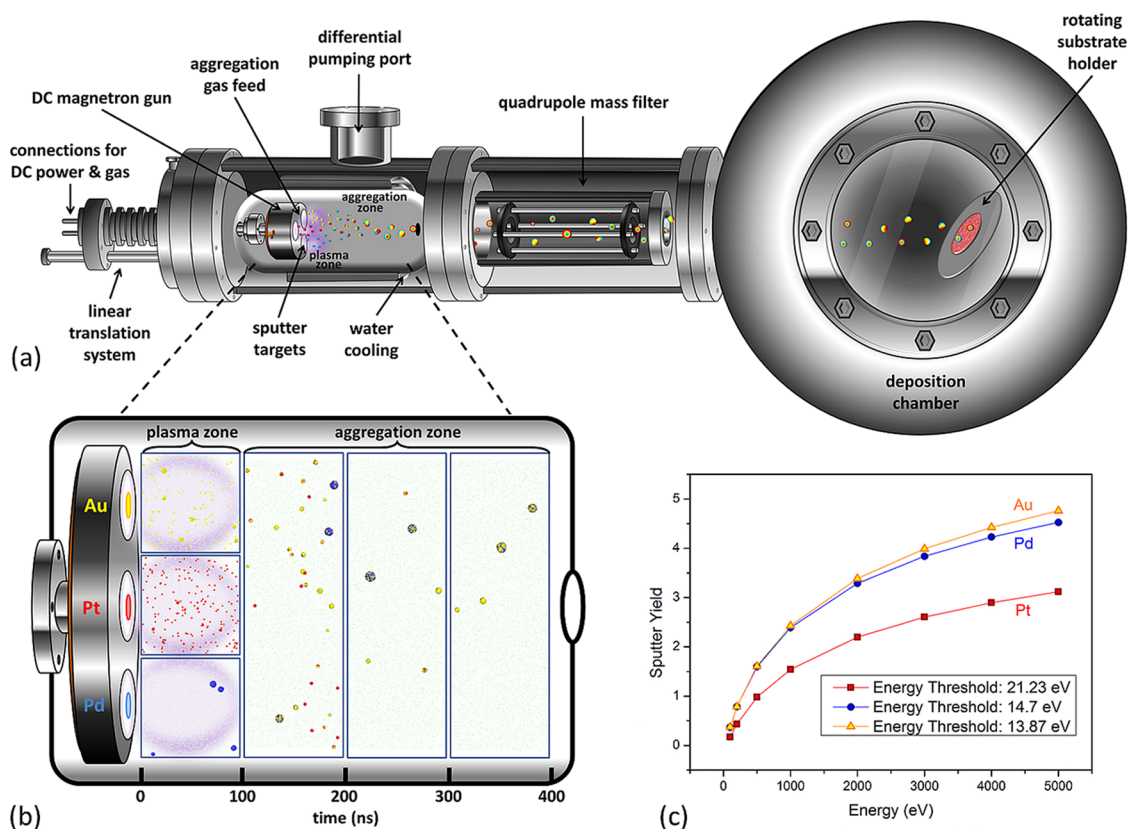
Figure 1. (a) Schematic representation of a magnetron-sputtering inert-gas-condensation system utilizing a triple-target configuration. (b) Schematic representation of the MD arrangement and its correspondence to the experimental setup. For the first 100 ns, individual nucleation of each element within plasma zones was simulated in a 1000 K Ar gas environment inside $50 \times 50 \times 50$ nm^3 simulation boxes. Next, growth within a room temperature aggregation zone represented by a single $150 \times 50 \times 50$ nm^3 simulation box was simulated for 300 ns. Au, Pt, Pd, and Ar atoms are represented by yellow, red, blue, and green spheres, respectively. (c) Calculated sputter yields for all three single-element targets for various energies, used as input for MD: Au and Pd have consistently similar yields, whereas the Pt yield is significantly lower, due to its higher sputter energy threshold.

Many studies focusing on bimetallic systems of these three elements (especially segregated systems with core@shell configurations) indicate a drastic enhancement of catalytic activity in various reactions and excellent electrochemical properties in general.[21−27] It was, therefore, expected that a suitable combination of these three noble metals would favorably modify the electronic structure of the nanoparticles and provide more active sites for enhanced catalytic activity.[28−33] Various studies focused on the Au−Pt−Pd system developed by some chemical route: by typical reduction of precursors and adjustment of decomposition kinetics to form multishell particles,[34,35] sol-immobilization,[36,37] fabrication from a poly(vinylpyrrolidone)-based aqueous solution,[31] electroless deposition,[38] etc. These syntheses enabled the formation of spherical, multishell Au@Pd@Pt nanoparticles,[34] nanoalloys,[38] Au@Pd@Pt nanocubes,[39] or even interesting trimetallic "nanoflowers".[40] Experimental studies clearly demonstrated these trimetallic clusters' improved chemical stability for fuel cell reactions[23,30] and impressive catalytic activity for the methanol oxidation reaction,[31,35,39,41] glucose oxidation,[42] selective oxidation of benzyl alcohol,[43] formic acid electro-oxidation,[34] electrochemical performance for oxygen reduction reaction,[40,44] etc. Simultaneously, computational simulation studies established that trimetallic clusters at thermodynamic equilibrium typically contain Au atoms at the surface, sometimes accompanied by Pd atoms, whereas Pt atoms usually occupy inner layers, preferably forming a

subsurface layer.[45,46] The main mechanisms responsible for the optimal chemical order are surface energy and elastic stress minimization and maximization of the number of high-strength bonds (i.e., Pt−Pt).[47,48] It should be stressed, however, that these studies concerned small clusters, typically on the order of a few tens or, at the extreme case, hundreds of atoms.

This study is the first to present fabrication of trimetallic Au−Pt−Pd nanoparticles through a gas-phase synthesis route. The main goal of this work was to engineer trimetallic Au−Pt−Pd nanoparticles by means of magnetron-sputtering inert-gas condensation.[49] To allow for a broad spectrum of relative compositions, three independent neighboring targets of Au, Pt, and Pd were utilized. We determined a specific combination of sputtering powers, which, through their resultant relative concentrations of sputtered atoms during nucleation, consistently led to the deposition of purely trimetallic nanoparticles. Several characterization techniques such as atomic force microscopy (AFM), X-ray photoelectron spectroscopy (XPS), and high-resolution (scanning) transmission electron microscopy [HR-(S)TEM] were used to investigate the structural and chemical orders of these nanoparticles. As Au, Pt, and Pd display similar lattice parameters, structural analysis was challenging; therefore, experimental studies were complemented with computational simulation studies. Predicting the structure of mixed-element nanoparticles is nontrivial due to its dependence on both size and complex energy landscape: to reach equilibrium, a multimetallic nanoparticle must

optimize both geometrical shape and chemical ordering. Nanoparticles grown by gas-phase aggregation are often trapped in metastable configurations due to the out-of-equilibrium conditions during growth; therefore, their configuration is determined not only by energetic but also by kinetic effects. Using molecular dynamics (MD) and Metropolis Monte Carlo (MMC) simulations, we were able to determine the equilibrium structural and chemical ordering of the particles, describe the metastability of the experimental clusters, and elucidate their formation mechanisms. We emphasize the paramount importance of early-stage nucleation as a limiting factor for the growth of multicomponent nanoparticles.

METHODS

Materials. The nanoparticles were fabricated by sputtering Au (purity >99.999%), Pt (purity >99.99%), and Pd (purity >99.95%) magnetron-sputtering targets 25 mm in diameter and 3 mm in thickness (Kurt J. Lesker, PA). As substrates for AFM and XPS measurements, undoped Si dice 5 × 5 mm in size with (100) orientation were used (MTI Corporation, CA). Copper frames with electron-transparent carbon-coated grids (400 mesh) and silicon nitride membranes were utilized as substrates for TEM/STEM-high angle annular dark field (HAADF) analysis (Ted Pella Inc., CA).

Nanoparticle Synthesis. Trimetallic nanoparticles were synthesized using a direct current (DC) magnetron-sputtering inert-gas aggregation system, schematically illustrated in Figure 1a. The deposition system consists of a multitarget nanocluster sputtering source, a quadrupole mass filter (QMF), and a deposition chamber. Au, Pt, and Pd sputtering targets were located side by side on an integrated magnetron-sputtering head in an equilateral triangle configuration. The initial base pressure was ~2.0 × 10^{-6} Pa. During deposition, pressures in the nanocluster aggregation zone and deposition chamber were ~25 and ~7.0 × 10^{-2} Pa, respectively. Ar gas flow rate and aggregation zone length were set at 70 sccm and 100 mm, respectively. A series of samples were produced keeping the Ar gas flow and aggregation length constant; the only parameter that was adjusted was the DC magnetron power applied independently on each target while co-sputtering (5−20 W). Nanoparticle sizes and compositions were monitored via in situ QMF feedback and, subsequently, by AFM/XPS characterization. The nanoparticles were deposited on either (holey) carbon-coated Cu grids or on 8 nm thick silicon nitride membranes. The substrate holder was rotated (at 2 rpm) to ensure homogeneous deposition. To obtain submonolayer coverage, the deposition time was limited to 3 min. After deposition, samples were transferred via a load lock chamber to a nitrogen-filled glovebox for storage before characterization experiments.

Characterization. A Bruker Multimode 8 AFM was used to analyze the topography of the samples, utilizing the NanoScopeV controller in tapping mode equipped with a triangular silicon nitride AFM tip (radius <10 nm, force constant: 0.35 N m^{-1}, resonant frequency: 65 kHz). The AFM system height "z" resolution and noise floor were <0.03 nm. Height distribution curves were extracted from the AFM images by built-in functions of the scanning probe processor software (SPIP 6.3.3, Image Metrology, Hørsholm, DK).

XPS measurements were performed in a Kratos AXIS-Ultra DLD Photoelectron spectrometer with a base pressure of 2 × 10^{-7} Pa and using a monochromatic Al Kα source (1486.6 eV); for quantification, the CasaXPS software was used. The Pd 3d, Au 4f, and Pt 4f core-level narrow spectra were recorded using a pass energy of 20 eV for high resolution. Full width at half-maximum values for Au, Pt, and Pd (0.83 eV,[50] 0.96 eV,[51] and 0.86 eV,[52] respectively) were imported into the software as constraints to relate the XPS spectra directly with their metallic widths. Charge correction was done against adventitious carbon C 1s (binding energy = 284.6 eV).

Regarding TEM experiments, nanoparticles were deposited on silicon nitride (Si$_3$N$_4$) thin films and the samples were exposed to air

before introduction to the microscope. HR-TEM was performed on an image-corrected FEI Titan E-TEM G2 operating at 300 kV, providing a spatial resolution of 0.1 nm. HAADF-STEM and energy-dispersive X-ray spectroscopy (EDS) measurements were carried out on a probe-corrected JEOL ARM 200F operated at 200 kV fitted with a large-angle EDS detector. HR-STEM mode provided a spatial resolution of 0.078 nm. HR-TEM/STEM micrographs and EDS data were acquired and processed using the Gatan Digital Micrograph environment.

Interatomic Potentials. For the computational part of this study, the classic embedded-atom method (EAM) interatomic potential developed by Foiles et al. was used to model the interactions between all three metallic species,[53] both for the nucleation MD and the demixing MD and MMC simulations. The heats of solution predicted by the potential follow the phase diagrams fairly well.[54] Energy differences between single impurities near a (100) surface and in the bulk of host materials, indicating surface segregation, are consistent with theoretical and experimental data.[55−57] However, small systems (>100 atoms) may have different structures compared with the extended system.[58] It was emphasized by the authors that in the cases related to Pt, the sign of the segregation energy differs for the two planes; this suggests that Pt atoms tend to segregate in the second atomic layer in the Au/Pt/Pd system. For sampling the potential energies, both the potential by Foiles et al.[53] and the potential by Adams et al.[59] were used for comparison purposes. The interactions between Ar atoms were modeled with the Lennard-Jones potential,[60] whereas the interactions between Ar and sputtered metal atoms were reproduced by the universal, purely repulsive potentials by Ziegler, Biersack, and Littmark.[61]

Molecular Dynamics Simulations. Two sets of MD runs were performed to simulate monometallic and trimetallic nanoparticle nucleation and growth. For the first set, the PARCAS parallel, classical MD code was used.[62−64] For the case of monometallic nucleation, various numbers of atoms corresponding to different magnetron powers (see Table 1) were introduced at random but isolated

Table 1. Numbers of Sputtered Atoms of Each Element Used for the MD Growth Simulations for Different Power Values

element	power (W)			
	5	10	15	20
Pt	500	800	1000	1100
Pd	900	1500	1800	1900
Au	900	1500	1800	1900

positions in a cubic box with a 50 nm side length and periodic boundary conditions. The initial temperature of all atoms was 3000 K. Each time an Ar atom passed through the simulation box boundaries, its temperature was reset to 300, 700, 1000, or 1500 K utilizing the Berendsen thermostat.[65] The metallic atoms were cooled by elastic collisions with colder Ar atoms; no other temperature control was used. Monometallic nucleation runs were 100 ns long.

For the case of trimetallic growth, we used numbers of atoms that corresponded to the particular sputtering power combination experimentally determined to be most effective for producing trimetallic nanoparticles. As summarized in our previous work,[66] we split the nucleation and growth process into two regions: plasma zone and aggregation zone. In the former region, monometallic nucleation of 500 Pt, 900 Au, and 1800 Pd atoms occurred for 100 ns inside individual simulation boxes of 50 × 50 × 50 nm^3 containing 5000 Ar gas atoms with a thermostat value set at 1000 K. This arrangement reproduces the physical separation of the hot plasma zones observed in our experimental setup. In the latter region, the three simulation boxes were combined into a single longer box, i.e., 150 × 50 × 50 nm^3, and mixed nanoparticle growth ensued for another 300 ns in an Ar environment at 300 K as continuation simulation runs; this way, we were also able to monitor mixed nanocluster coalescence. This

MD run arrangement is schematically summarized in Figure 1b, superimposed with MD visualization snapshots after every 100 ns.

The setup of the second set of monometallic nucleation and growth simulations was similar, but the runs were performed with LAMMPS.[67] 3125 metallic atoms (Au, Pt, or Pd) and either 12 500 or 100 000 Ar atoms were introduced in 100 × 100 × 100 or 200 × 200 × 200 nm^3 simulation boxes. The initial temperature of metallic atoms was 900 K. A Nosé–Hoover thermostat, set at 300 K, was used for the Ar gas.[68,69]

For the simulated annealing study of small monometallic clusters of up to 12 atoms, the formation energies were calculated after 100 cycles of fast heating (up to 2500 K) and minimization to the local minimum using the conjugate gradient method.[70] Subsequently, the lowest energy state was selected.

Monte Carlo Simulations. Monte Carlo simulations were performed to investigate the equilibrium chemical order of the bimetallic and trimetallic nanoparticles. Pairs of atoms of different types were picked randomly, and their types were swapped using the Metropolis criterion. After each exchange, the system was locally relaxed by MD to the closest local minimum. As such, the potential energy landscape was sampled according to the "basin hopping" global optimization algorithm.[71,72] All simulation snapshots are visualized using OVITO.[73]

■ RESULTS AND DISCUSSION

Theoretical Growth of Monometallic Nanoparticles. Recently, we reported on the formation of multicomponent nanoparticles via a versatile co-sputtering gas-condensation method, schematically shown in Figure 1a, utilizing a multitarget nanocluster sputtering source, a quadrupole mass filter (QMF), and a deposition chamber.[9,74−77] We showed that by concurrent magnetron sputtering from neighboring targets, one can vary the chemical composition of the fabricated nanoparticles by simply adjusting the sputtering powers at the respective targets.[74] In this setup, mixed-element nanoparticles mainly grow as a result of primary single-element cluster coalescence at a later stage of the nucleation and growth process, away from the targets and the hot plasma regions surrounding them.[74]

Therefore, we first explored the monometallic growth of each of the constituents of the desired trimetallic nanoparticles under identical sputtering conditions (pressures in the sputtering reactor, Ar flow, and aggregation zone length). The theoretically expected yield for each element is shown in Figure 1c, as given by a sputter yield calculator[78] based on species-dependent energy thresholds for sputtering and empirical equations for yields at normal incidence.[79] A key finding from this analysis is that the Pt yield is considerably lower than those of Au and Pd.

To guide our experimental study, after an initial benchmarking of the interatomic potential used (Figure S1), we performed classical MD simulations of monometallic nanoparticle nucleation and growth from the gas phase. The challenge for the MD simulation was to reproduce the experimental aggregation procedure as accurately as possible; therefore, we assigned a number of sputtered atoms to each specific magnetron power used experimentally (see below for the growth of trimetallic nanoparticles) based on the relative sputtering yields of Figure 1c (within necessary approximations), assuming a sputtering energy of ∼220 eV. The numbers of atoms used in our simulations are summarized in Table 1; we kept them relatively small for low computational cost but large enough to produce a significant number of nanoparticles so that we could analyze the growth kinetics between different species. The box size was 50 × 50 × 50 nm^3, and there were

5000 Ar atoms in each run so that equivalent cooling conditions were applied.

For each individual element, we varied two independent parameters: the temperature of the Ar gas thermostat (see Methods section) and the magnetron power. This way, we were able to investigate a broad spectrum of possible thermal environments during growth, which decisively affect the morphologies of the resultant nanoparticles.[80] The temperature and potential energy evolution of exemplary MD simulation runs is presented in Figure 2a; the temperature
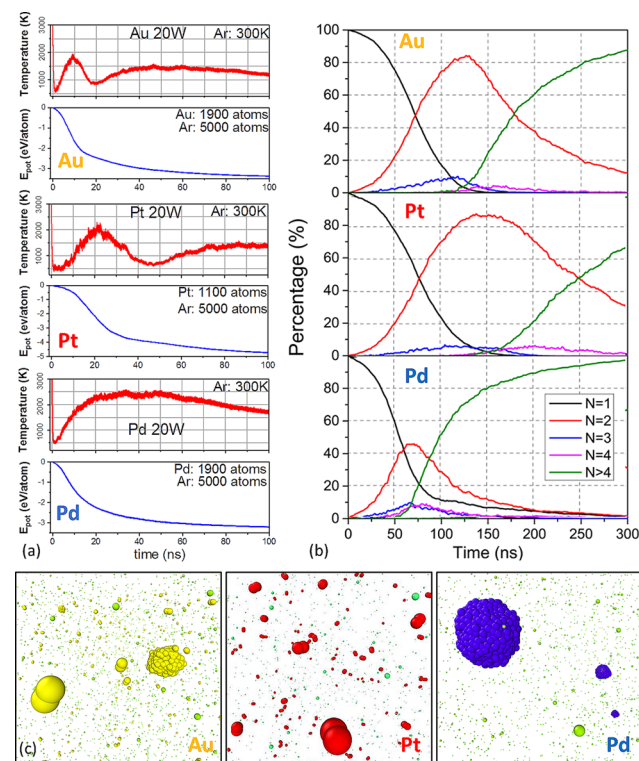

Figure 2. (a) Temperature and potential energy evolution graphs for Au, Pt, and Pd sputtered with 20 W in a room temperature Ar environment. The temperature spikes early on for Au and Pt correspond to an initial nucleation of dimers, which is not immediately followed by further growth. Instead, Pd clusters of larger sizes can readily form, leading to a high and broad temperature peak. (b) Percentage of atoms of each species bound in monomers, dimers, trimers, etc. as a function of time during MD simulations of gas condensation. Clearly, Au and Pt dimers reach much higher percentages and have much longer lifetimes compared with Pd dimers. (c) Snapshots from MD simulations of monometallic nucleation and growth at 1500 K Ar thermostat temperature and a sputtering power of 20 W after 100 ns. Au, Pt, Pd, and Ar atoms are represented by yellow, red, blue, and green spheres, respectively. Clearly, a vast majority of Pt atoms are still trapped in dimer cluster seeds, whereas large Pd clusters are already formed. The nucleation rate of Au is in between those of Pd and Pt.

increase and potential energy decrease are fingerprints of bond formations, indicating nucleation and growth of nanoclusters. Snapshots after 100 ns of simulation runs are shown in Figure S2 for all three atomic species for the two extreme power values used (i.e., 5 and 20 W) and for three different Ar gas thermostat temperatures (i.e., 700, 1000, and 1500 K). The effect of magnetron power and Ar temperature is further demonstrated in Figure S3. Higher power values led to denser sputtered gases, resulting in faster nanocluster formation in

almost all cases (see Figures S2 and S3a). This is verified by the number of clusters of non-negligible sizes present at each snapshot (most clearly in Au at 1000 K). A noticeable exception appears for Pt at 1500 K, where an increase in the number of atoms from 500 to 800 had no discernible effect on the aggregation kinetics; another rate-controlling mechanism became more important, as will be discussed below. Furthermore, a lower Ar gas temperature generally speeds up the growth process, as it provides more efficient cooling,[81] although the temperature effect is not always profound (see Figure S3b).

The most striking result is that Pd shows a tendency to nucleate remarkably faster than the other two materials. After Pd, Au nucleates the second fastest and Pt resists cluster formation the longest, especially at high temperatures and low atomic densities. As a result, there is a marked distinction between the temperature profile of Pd and those of Au and Pt (see Figure 2a). For the latter two, a sharp peak can be identified at ∼10 and ∼20 ns, respectively, followed by a second, lower and much wider peak. The sharp peaks are the result of rapid formation of single bonds pairing the atoms in dimers, whereas the wider ones are associated with the addition of extra atoms toward larger nuclei. In contrast, the temperature evolution of Pd shows a single strong and broad peak since temperature spikes due to first, second, third, etc. bond formations merge owing to the higher nucleation rate. This unexpected result is further scrutinized in Figure S4, examining parameters associated with the experimental setup such as Ar gas pressure and metal-to-inert-gas atomic ratio.

The lifetimes of clusters containing 1, 2, 3, 4, or >4 atoms for each species are shown in Figure 2b. Clearly, Au and Pt dimers not only reach much higher percentages of atoms bound in them than Pd dimers but they also significantly outlive them. In addition, the formation of Pd clusters of a larger size (i.e., >4) starts much earlier than that of Au or Pt. As a consequence, large Au and Pt clusters are mainly formed by subsequent addition of dimers rather than deposition of individual adatoms, as verified by the mirror symmetry in the decreasing "N = 2" and increasing "N > 4" curves for Au and Pt after 120 ns in Figure 2b; this effect is not observed for Pd. MD simulation snapshots for all three species confirm these differences in nucleation rates, showing that after 100 ns all Pd atoms are already bound in large clusters, whereas, in contrast, practically all Pt atoms are still trapped in dimers. Au exhibits intermediate behavior, demonstrating a great number of diatomic nuclei, whereas the presence of larger clusters is scarce (Figure 2c).

To understand the reason behind this distinct difference in nucleation behavior between Pd and Au or Pt, we calculated the potential energy per atom for clusters of all three species containing 2−12 atoms. For each cluster, we performed 100 cycles of fast heating up to 2500 K and subsequent quenching to 0 K, after which we selected the configurations of the lowest energy states; a comparison between them is shown in Figure 3. To verify our result, we repeated the same simulations performed with the original potential[53] by utilizing another embedded-atom method (EAM) interatomic potential.[59] Oscillations in energy values between clusters containing odd and even numbers of Au and Pt atoms are clearly demonstrated for both potentials used; as a result, Au and Pt dimers appear more stable than the trimers, which explains their pronounced and prolonged presence during nucleation and growth. This phenomenon is more prominent for Pt, in
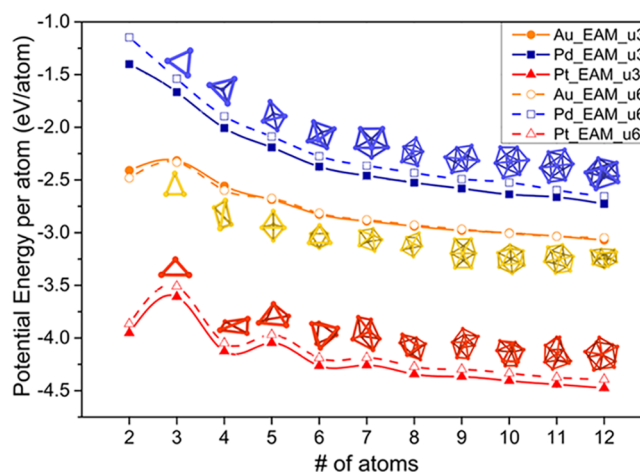

Figure 3. Potential energy per atom as a function of the number of atoms for low-nuclearity monometallic clusters consisting of Au, Pt, or Pd atoms, given by two EAM-type potentials.[53,59] Enhanced stability is indicated for Au and Pt dimers compared to their respective trimers. In contrast, the stability of Pd clusters increases monotonically with size.

agreement with its aforementioned nucleation behavior. In contrast, the stability of Pd clusters grows monotonically, allowing for unobstructed, and, thus, faster, growth of Pd nanoparticles of larger sizes.

Similar trends in the evolution of the cohesive energy of Au/Pt, Au/Pd, and Pd clusters have been reported in various ab initio studies[82−85] and attributed to the difference in the electronic configurations of the atoms. All three elements are transition metals, but although Au and Pt share open-shell $6s^1$ valence configurations, forming stable bonds characterized by a σ doubly occupied highest occupied molecular orbital (HOMO) and a σ^* lowest unoccupied molecular orbital (LUMO), Pd has a $4d^{10}$ configuration, which translates into 4d electronic density being promoted to 5s to form stable bonds. The energy oscillations observed for Au and Pt clusters can be attributed to the alternation between resultant stable closed-shell and less-stable open-shell configurations. However, even within the density functional theory framework, there is no general consensus regarding the shapes and ground states of transition-metal clusters of low nuclearity, as different studies reported contradicting results, mainly due to their sensitivity on the selection of basis sets and approximations.[86] It should be noted, however, that even studies that did not reproduce this oscillatory behavior for the clusters' binding energies (such as, e.g., ref 87 for Pt clusters) reported similar oscillatory behavior for other properties such as the HOMO−LUMO bandgap, a parameter that affects the chemical stability, or the magnetic moments.[88]

It should be underlined that neither of EAM-type interatomic potentials used in this work is explicitly designed to reproduce such behavior, but both are rather fitted to bulk properties.[53,59] The nature of the embedding function implies the presence of metallic bonds as a result of the presence of an electron cloud within the crystal, whereas the bonds during the initial stages of gas-phase nucleation are, in principle, covalent. The reproduction of the experimental nucleation behavior and ab initio energetics calculations may be initially considered fortuitous; however, a possible explanation lies on the fact that the embedding functions and pair interactions were based on first-principles calculations that take the electronic structure
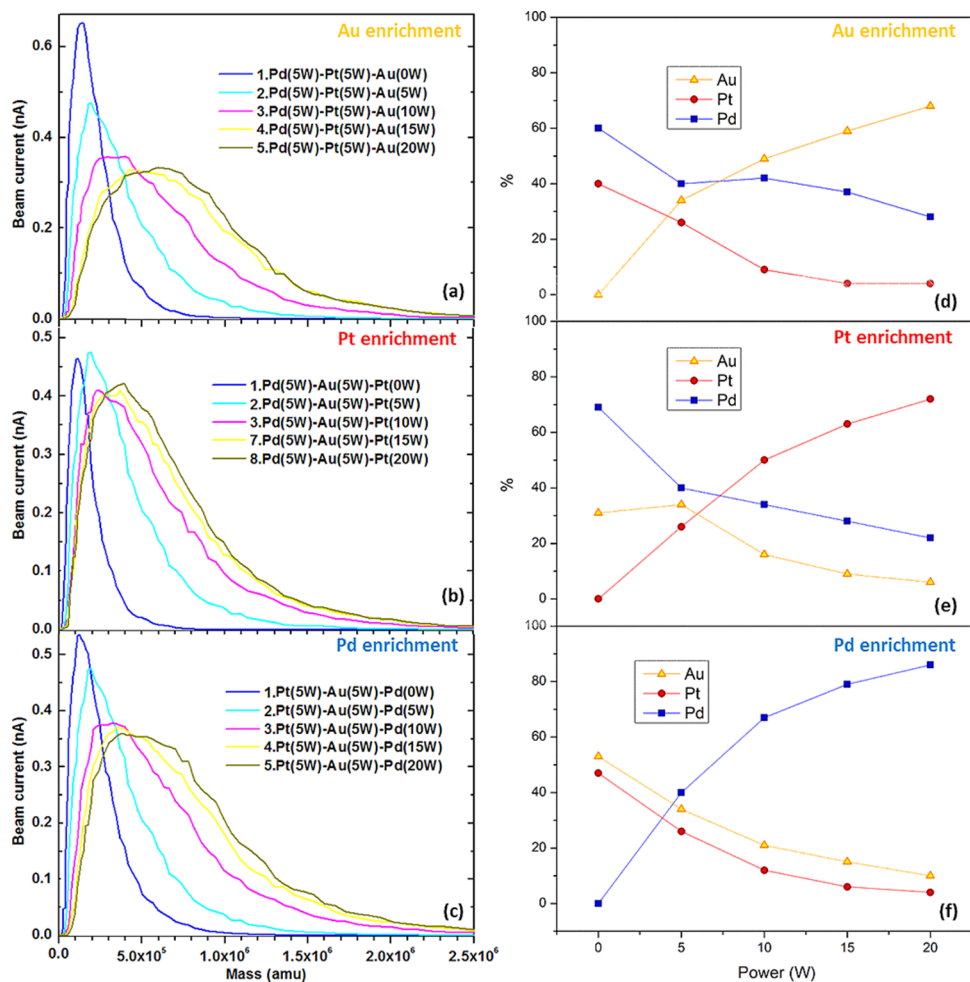
Figure 4. Comparison of QMF profiles of binary and ternary nanoparticles with increasing (a) Au, (b) Pd, and (c) Pt concentrations. The distributions shift toward larger sizes and become wider as the sputtering power increases from 0 to 20 W in 5 W increments for the target of the respective enriched element. The powers of the remaining two targets remained fixed at 5 W. Quantification from XPS analysis of surface composition in atom %. for each enrichment series: (d) Au, (e) Pd, and (f) Pt. Again, Pd is found to be the easiest element to form nanoparticles.

into account.[53] Indeed, the Foiles EAM potential predicts ground states of small Pt clusters that resemble an ensemble of dimers; such configurations are also predicted ab initio for Au by Zanti et al.[82]

Experimental Growth of Trimetallic Nanoparticles. Taking the primary theoretical results of the monometallic growth of individual Au, Pt, and Pd nanoparticles into account, we co-sputtered all three elements concurrently. Three series of samples were produced keeping all deposition parameters constant, except for the DC power applied independently to each magnetron. For each of these series, the DC power value of one of the targets was increased from 0 to 20 W, as indicated in Table 1, whereas DC powers of 5 W were constantly used for the remaining two targets. This led to enrichment in the concentration of one specific element per series. The size and composition of the deposited nanoparticles were checked in flight via QMF feedback, as shown in Figure 4a−c, and post-deposition by AFM, as presented in Figure S5. To obtain submonolayer nanoparticle coverage and restrict Smoluchow-ski ripening, the deposition time was limited to 3 min.

Quantitative analysis of the chemical composition of each sample was performed via X-ray photoelectron spectroscopy (XPS). Although XPS is, in principle, a surface technique, the small dimensions of the clusters meant that the overall sample

was sufficiently probed. Figure 4d−f shows the percentage of atoms of each species present with increasing magnetron power of individual Au, Pt, and Pd targets, respectively. It should be stressed that these percentages correspond to the presence of atoms in the ensemble and not to individual nanoparticles. Interestingly, the percentage of Au when sputtered with the same power as Pd is consistently lower than that of Pd; instead, it is rather comparable with the percentage of Pt (as more clearly illustrated in Figure S6). Evidently, this corresponds to its low clustering rate as shown by MD above and not to its high sputter yield, indicating that this is the primary limiting factor in the nanoparticle fabrication process.

Therefore, to obtain consistently trimetallic nanoparticles, one needs to form seeds where Au and Pt sputtered atoms can nucleate on. Pd, with its faster nucleation rate, can play this role forming initially monometallic nuclei where Au and Pt adatoms (or, rather, dimers, as previously discussed) can attach to. As a result, a higher Pd sputtering power is necessary to increase the number of potential trimetallic nucleation sites. The Au-5W/Pt-5W/Pd-15W sample produced practically solely trimetallic nanoparticles, as indicated by XPS spectra showing strong interaction among the three atomic species (Figure S7) and verified by the TEM survey of more than 50

nanoparticles including the smallest ones observed. Utilizing a higher Pd power (i.e., 20 W) resulted in excessive amounts of Pd atoms in the aggregation zone and the ensuing growth of monometallic Pd nanoparticles, too. Although it is unlikely that there exists only one specific sputter power combination, which can lead to the growth of uniformly trimetallic nanoparticles, it is important to emphasize that a certain balance has to be reached to avoid surpluses or deficits of any atomic species.

Theoretical Growth of Trimetallic Nanoparticles. We utilized MD to simulate the growth of trimetallic nanoparticles, using for each species numbers of atoms corresponding to the sputtering power Au-5W/Pt-5W/Pd-15W. We repeated the MD nucleation and growth process four times, starting from different random configurations. Through visualization snapshots of MD runs (such as those in Figure 1b), we could follow the temporal evolution of the gas-condensation process from the primordial monometallic nuclei and small single- or mixed-element nanoclusters all the way toward larger trimetallic nanoparticles. By the end of this series of simulation runs, a whole galaxy of nanoparticles of various sizes, shapes, and chemical configurations were produced; a representative sample is shown in Figure 5. In the first column, all atom types are depicted in white to emphasize the shapes of the nanoparticles. For small clusters, the icosahedral shape is the most common; this is clear as the clusters are viewed along their fivefold axes (also their twofold axes in some instances; see small insets). It should be mentioned that due to the random nature of the gas-condensation process, the growth of highly symmetrical icosahedral nanoparticles is not attributed to the occurrence of any magic numbers, either of the Mackay or the anti-Mackay series $\left(N_{Ih}^{M} = \frac{1}{3}(10k^3 - 15k^2 + 11k - 3)\right.$, $k \geq 1$ and $N_{Ih}^{aM}(k) = N_{Ih}^{M}(k) - 10(k-2)$, $k \geq 3$, respectively, where k is the number of the atomic layers).[89] For larger sizes, there is a tendency toward single-crystalline face-centered cubic (FCC) clusters, either in near-truncated-octahedral or spheroidal shapes. This behavior is expected, as crystalline motifs become increasingly favorable when the nanoparticle size increases and the macroscopic bulk limit is approached.[89] However, this is not always the case, as indicated by the large equiatomic icosahedron of the bottom row.

The middle two columns reveal the atomic composition and chemical ordering of the nanoparticles: Au, Pt, and Pd atoms are depicted in yellow, red, and blue, respectively. Small clusters appear either Pd- or Au-rich; larger ones are mainly Pd-rich or roughly equiatomic. Au atoms consistently show a tendency to segregate to the surface and create a single-layer envelope surrounding the particles (see, e.g., rows 1−4). Pt atoms always remain one layer shy of the outer shell, and they either fill the core, when their concentration is high enough, or prefer to occupy subsurface sites. For the former case, see, e.g., the top four rows; the inset in row 2 has Pt atoms slightly exaggerated in size to emphasize their presence in the subsurface layer. For the latter case, see insets of rows 8−9, where a slice through the clusters' equatorial plane is shown. Pd atoms can be found in every layer of the nanoparticles due to their large amount. Interestingly, there is no direct correlation of the atomic composition and chemical ordering of the nanoparticles with their shape or size.

Finally, the crystallographic phase of each nanoparticle can be identified in the last column: atoms depicted in green
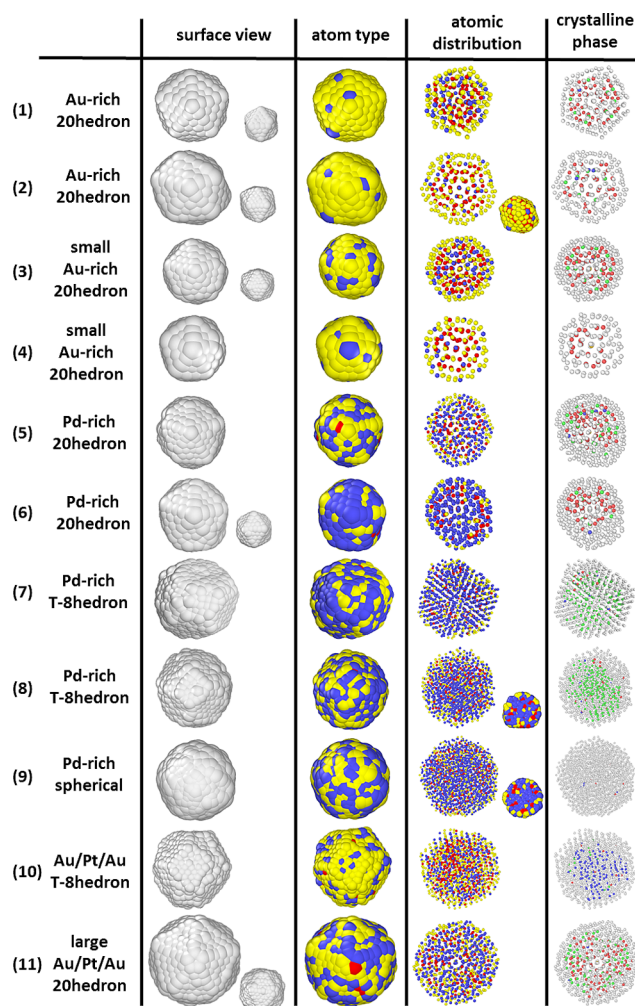

Figure 5. Visualization of all nanoparticles grown by MD simulations according to the scheme shown in Figure 1b, revealing a variety of structures. In the first column, all atoms appear white to demonstrate the shapes of the particles; icosahedral, truncated-octahedral, and spherical particles are shown (atom sizes are not to scale). The small insets depict the same icosahedral particles viewed along their twofold axes. The second column shows the same particles from an identical viewpoint, indicating their species: Au, Pt, and Pd atoms are represented by yellow, red, and blue spheres, respectively. In the third column, atom size is reduced to enable view through the particles and reveal their intrinsic structures. The small insets emphasize the presence of Pt in the subsurface layer. The crystalline phase of the particles is revealed in the last column. Atoms belonging to an FCC, body-centered cubic (BCC), and amorphous structures appear green, blue, and white, respectively. Red atoms reveal twin boundaries.

belong to FCC structures (see, e.g., rows 7 and 8), whereas red atoms indicate the existence of twin boundaries (see, e.g., top six rows). There are also deviations from these patterns, with a near-spherical nanoparticle in an amorphous state (atoms depicted in white) and one roughly truncated-octahedral nanoparticle appearing mainly BCC (atoms depicted in blue). This is only temporary and, in principle, expected since there is no guarantee that all nanoparticles reach equilibrium within the timeframe of our simulations. It should be mentioned that in this column, atom sizes are reduced to enable observation through the clusters so as to demonstrate the fivefold symmetry of the twinned clusters. Also, note that surface
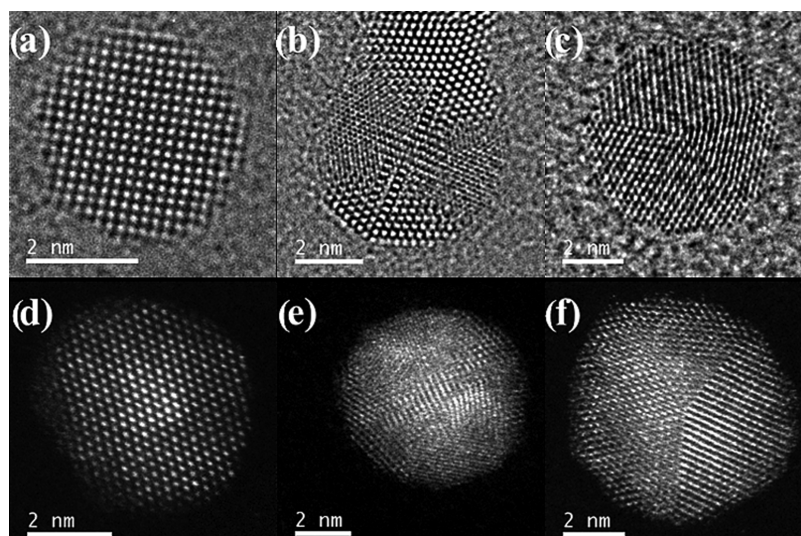
Figure 6. HR-TEM micrographs reveal the physical ordering of nanoparticles from the trimetallic Au-5W/Pt-5W/Pd-15W sample: (a) FCC particle viewed along its [100] zone axis, (b) icosahedral particles viewed along their twofold symmetry axes, and (c) decahedral particle viewed along its fivefold symmetry axis. STEM-HAADF micrographs contain more information regarding the chemical ordering of the particles: (d) FCC particle viewed along its [101] zone axis, (e) icosahedron viewed along its twofold symmetry axis, and (f) fivefold twinned nanoparticle (decahedron).
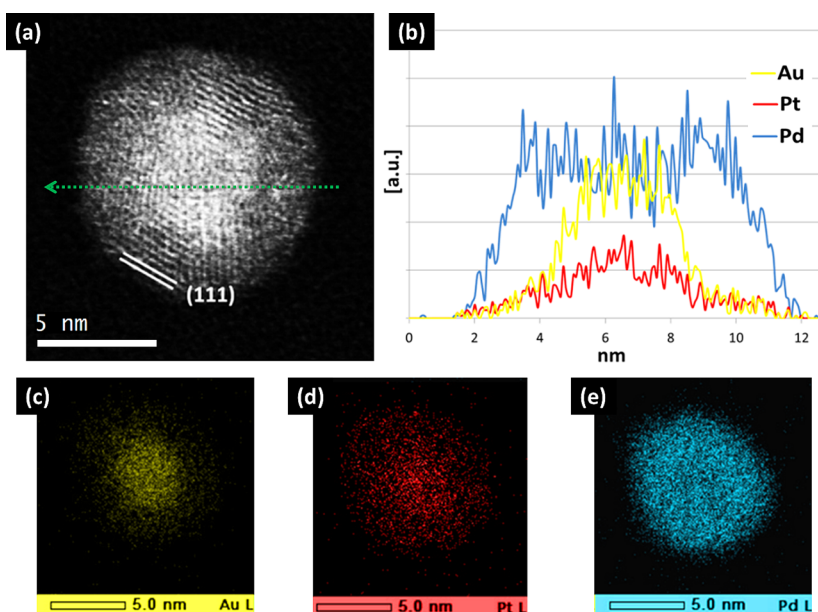

Figure 7. (a) HR-STEM-HAADF micrograph of a multifaceted nanoparticle displaying fivefold symmetry and (b) its corresponding EDS line scan across the nanoparticle diameter (dashed green line), indicating the Au/Pt-rich core@Pd-rich shell configuration. (c−e) Local elemental mapping by EDS verifying the core−shell structure (the intensity corresponds to counts).

atoms always appear white due to their limited coordination number; this does not mean that they are in an amorphous state.

Characterization of Trimetallic Nanoparticles. We performed HR-TEM characterization to investigate the physical order of experimentally fabricated nanoparticles of the trimetallic Au-5W/Pt-5W/Pd-15W sample. As reported in Figure 6, this analysis revealed well-crystallized nanoparticles in several structures. Figure 6a depicts an exemplary single-crystal FCC particle oriented along the [100] zone axis. In Figure 6b, icosahedral nanoparticles exhibiting twofold symmetry display tetrahedral facets oriented along the [110] and [111] directions.[90] Decahedral nanoparticles were also identified,

such as that of Figure 6c, which is oriented along the fivefold axis and limited by {111} facets.

Chemical order analysis of the nanoparticles is more challenging since all elements crystallize in the FCC phase in the bulk and Pt and Pd have similar lattice parameters (a_{Pt} = 3.916 Å and a_{Pd} = 3.881 Å), which prohibits distinguishing them by spatial resolution. Fast Fourier transform (FFT) analysis from HR-TEM images revealed no numerical Bragg spots of the $L1_0$ or $L1_2$ superstructures typical of an ordered alloy. However, although HR-TEM does not enable distinguishing the Pt from the Pd lattice, scanning-TEM in high-angle annular dark-field (HAADF-STEM) mode provides a signal proportional to the atomic charge number Z (Z_{Pd} = 46,

$Z_{Pt} = 78$, and $Z_{Au} = 79$). Thus, the contrast in STEM mode can directly signify the atomic composition.[91]

For example, the single-crystal FCC particle oriented along the [101] zone axis, displayed in Figure 6d, exhibits a clear contrast between the core and the shell. The high signal intensity in the core can be attributed to either Au or Pt (or both) since the atomic numbers of these elements differ by only one nucleon; the shell, which displays low intensity, most likely corresponds to Pd enrichment. However, one can still observe a high-intensity signal from some atoms in the shell region. Figure S8 displays the intensity of the electronic density along the (111) planes across the nanoparticle and along the (020) planes from the shell. The intensity profile across the body of the nanoparticle confirms the high atomic numbers in the core region, whereas the profile on (020) planes of the shell divulges some isolated atoms with a higher intensity. This reveals the localization of Au and/or Pt in the core region along with some isolated atoms in random positions in the shell, whereas Pd occupies the main part of the nanoparticle.

The icosahedron depicted in Figure 6e demonstrating its twofold symmetry reveals a bright core and low signal intensity in the shell. However, one can still observe on the surface isolated atoms on the (111) planes displaying a higher intensity related to Au or Pt. Finally, the exemplary decahedral nanoparticle displayed in Figure 6f shows different domains with a higher intensity along the shell and partially on three facets.

To recognize what determines the chemical order of each cluster, energy-dispersive X-ray spectroscopy (EDS) analysis was carried out to identify and localize specific energies related to each element. The characteristic X-ray energies of Au $M\alpha$ and Pt $M\alpha$ are similar due to their similar atomic numbers, which results in an overlap of $M\alpha$ peaks on their EDS spectra.[92] To overcome this problem, the $L\alpha$ emission line was used to differentiate Au and Pt peaks, despite the loss of signal intensity.

A chemical mapping of a multiply twinned polyhedral nanoparticle and the corresponding line profile recorded across its diameter are reported in Figure 7; the cluster is limited by low-surface-energy (111) facets. The HR-STEM-HAADF image of Figure 7a displays higher intensity in the core, which can be attributed to the presence of Au and/or Pt. A line scan along the dashed green line displays a compositional gradient from the core to the shell, with the Pd concentration showing a higher intensity in the shell region and a small decrease in the core region (Figure 7b). Conversely, the core region shows an important Au and Pt enrichment compared to the surface. The elemental mapping of Figure 7c−e confirms the Au−Pt-rich core@Pd-rich shell configuration.

A quantitative analysis for this nanoparticle gives an estimated elemental composition of Au 0.17:Pt 0.05:Pd 0.78. The high atomic concentration of Pd and the low percentage of Au and Pt are correlated with the sputtering power used for each magnetron target. Interestingly, this particle shows almost identical composition as the overall sample. In agreement with the previous discussion, the Au/Pt atomic ratio in this nanoparticle is >1 (namely, ∼3.4), despite the same sputtering power used for both targets. The atomic concentration of Pd reaches 0.83 in the surface region but decreases to 0.56 in the core region, consistent with a core−shell distribution.

Similar EDS analysis was performed on spherical single-crystalline nanoparticles, as well. The exemplary HR-STEM-HAADF micrograph of Figure 8 reveals a cluster adopting
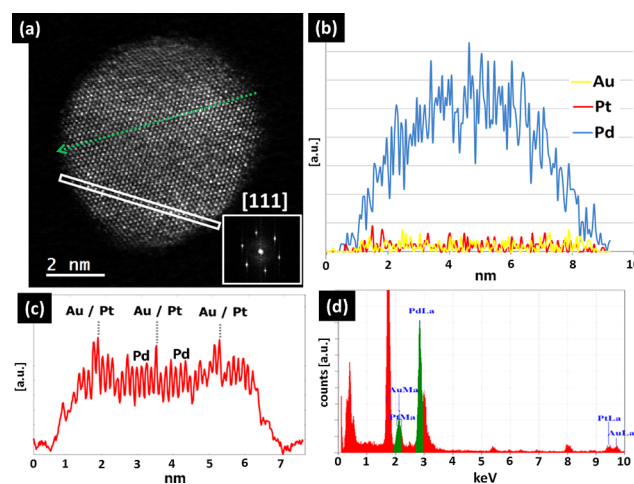

Figure 8. (a) HR-STEM-HAADF micrograph of a spherical, single-crystal nanoparticle (FFT displayed in the inset) and (b) its corresponding EDS line scan across the dashed green line, showing the relative concentrations of each element. (c) HR-STEM-HAADF contrast profile extracted along the white frame in (a), indicating a random solid solution of Au and Pt dopants inside a Pd matrix. (d) EDS spectrum attesting the presence of all three metals within the nanoparticle.

FCC structure, oriented along the [111] zone axis (an FFT of the particle is displayed in the inset). The EDS spectrum of Figure 8d confirms the presence of all three metals within the nanoparticle, whereas the EDS profile across the nanoparticle shown in Figure 8b underlines the very low concentration of Au and Pt. A HR-STEM-HAADF contrast profile is also plotted across the particle, perpendicular to $(\overline{2}02)$ planes (Figure 8c), revealing some fluctuation in intensity; atomic columns with higher intensity can be assigned to relative Au and/or Pt enrichment, whereas atomic columns with lower intensity should mostly consist of Pd. This particle clearly displays a random solid solution configuration, with Au and/or Pt dopants obtaining substitutional interstitial positions inside a Pd matrix.

Examination of more nanoparticles revealed no discernible interdependence between physical and chemical ordering. For example, Figure S9 shows a spheroidal, single-crystal particle with clear core−shell segregation, whereas Figure S10 shows a polyhedral random nanoalloy. Instead, elemental composition determines the mixing or nonmixing pattern for each particle, as segregation is evident only in particles with non-negligible amounts of Au and/or Pt atoms.

From an energetics point of view, it was expected that differences in atomic sizes (i.e., empirical atomic radii of $R_{Au} = 144$ pm, $R_{Pt} = 139$ pm, and $R_{Pd} = 137$ pm) can have an effect on the chemical ordering of individual clusters. The larger size of Au atoms, compared to those of Pt and Pd atoms, can induce some elastic stress in the lattice and result in larger atoms segregating to the surface to release elastic energy.[45] Likewise, the surface energy of Au is lower than those of Pt and Pd (typically 1.5 J m^{-2} for Au, 2.489 J m^{-2} for Pt, and 2.003 J m^{-2} for Pd), which was also expected to drive Au atoms to the surface to minimize the total energy of the system.[45,48] To resolve this issue, we investigated the energetically favorable structures of Au−Pt−Pd trimetallic nanoparticles of shapes and compositions relevant to our experimentally grown particles by combined MD and MMC simulations efficiently sampling the potential energy landscape. In agreement with the

previous literature, all stable structures display Au−Pd mixed surfaces and a Pd core, with Pt atoms occupying subsurface positions, preferably in (100) facets and twin boundary sites.[45,46]

Therefore, the experimentally observed (Au−Pt)@Pd core−shell distribution is metastable according to the aforementioned energetic considerations where Au is expected to segregate to the surface. Metastability can be attributed to the randomness of the gas-condensation process, where trimetallic nanoparticles form by coalescence of simpler clusters. For example, most of the Pt atoms appear in the core of the nanoparticle. The cohesive energies of Au, Pt, and Pd being 3.81, 5.84, and 3.89 eV, respectively, mean that Pt−Pt bonds are the strongest bonds displayed in this system. A preformed Pt cluster coalescing with another cluster of different composition (or being covered by different adatoms) may not dissolve but remain rather intact in the core,[47] covered by the other atoms wetting its surface.[74] Fast quenching upon deposition means that there is a high probability for these particles to be trapped in such metastable configurations. Similar metastability is not observed in our MD study of trimetallic growth since most simulated nanoparticles reproduce the energetically favorable chemical ordering predicted by MD and MMC due to their small sizes (compared to their experimental counterparts) enabling them to approach equilibrium.

CONCLUSIONS

In this contribution, we engineered by gas-phase synthesis complex trimetallic Au−Pt−Pd nanoalloys, which are usually fabricated by wet chemistry methods. By means of classical MD simulations, we investigated the parameters that govern the nucleation and growth of each element into monometallic clusters and alloy nanoparticles; such parameters include the Ar gas pressure and temperature and the relative atomic ratios between the sputtered species and the Ar gas. Our results reveal that the clustering rate and not the sputter yield of each elemental species is the primary limiting factor in the mixed nanoparticle fabrication process. We propose that the electronic structures of Au and Pt make them linger in dimeric configurations during nucleation; in contrast, the electronic structure of Pd enables its fast monometallic growth. Using these results, we were able to consistently fabricate trimetallic nanoalloys enriched in Pd. Our experimentally grown nanoparticles display alloy core@Pd-rich shell structures, which we demonstrated as metastable by means of MMC simulations, revealing the equilibrium structures of such systems. Our synthesis strategy can be applied for a wide range of trimetallic systems; furthermore, it is general and flexible enough to pave the way for the synthesis of even more complex nanoalloys containing four, five, or more elements for targeted applications.

ASSOCIATED CONTENT

Ⓢ Supporting Information

The Supporting Information is available free of charge on the ACS Publications website at DOI: 10.1021/acs.chemmater.9b00129.

> Monte Carlo simulations of energetically favorable structures of nanoparticles with equiatomic and experimentally derived compositions; additional data on the MD growth of monometallic nanoparticles; and

supporting AFM, XPS, and HR-STEM characterization data (PDF)

AUTHOR INFORMATION

Corresponding Authors
*E-mail: pgrammatikopoulos@oist.jp (P.G.).
*E-mail: mukhles@oist.jp (M.S.).

ORCID
Panagiotis Grammatikopoulos: 0000-0002-0057-6339
Vidyadhar Singh: 0000-0001-8164-4534
Stephan Steinhauer: 0000-0001-6875-6849
Mukhles Sowwan: 0000-0002-0211-2124

Notes
The authors declare no competing financial interest.

REFERENCES

(1) Gas-Phase Synthesis of Nanoparticles; Huttel, Y., Ed.; Wiley-VCH: Weinheim, 2017.

(2) Foster, D. M.; Ferrando, R.; Palmer, R. E. Experimental Determination of the Energy Difference between Competing Isomers of Deposited, Size-Selected Gold Nanoclusters. Nat. Commun. 2018, 9, No. 1323.

(3) Xu, Y.-H.; Wang, J.-P. Direct Gas-Phase Synthesis of Heterostructured Nanoparticles through Phase Separation and Surface Segregation. Adv. Mater 2008, 20, 994−999.

(4) Brault, P.; Neyts, E. C. Molecular Dynamics Simulations of Supported Metal Nanocatalyst Formation by Plasma Sputtering. Catal. Today 2015, 256, 3−12.

(5) Zhao, J.; Baibuz, E.; Vernieres, J.; Grammatikopoulos, P.; Jansson, V.; Nagel, M.; Steinhauer, S.; Sowwan, M.; Kuronen, A.; Nordlund, K.; Djurabekova, F. Formation Mechanism of Fe Nanocubes by Magnetron Sputtering Inert Gas Condensation. ACS Nano 2016, 10, 4684−4694.

(6) Palmer, R. E.; Cao, L.; Yin, F. Note: Proof of Principle of a New Type of Cluster Beam Source with Potential for Scale-up. Rev. Sci. Instrum. 2016, 87, No. 046103.

(7) Krishnan, G.; Verheijen, M. A.; ten Brink, G. H.; Palasantzas, G.; Kooi, B. J. Tuning Structural Motifs and Alloying of Bulk Immiscible Mo-Cu Bimetallic Nanoparticles by Gas-Phase Synthesis. Nanoscale 2013, 5, 5375−5383.

(8) Benelmekki, M. Designing Hybrid Nanoparticles; Morgan & Claypool Publishers: San Rafael, 2015.

(9) Benelmekki, M.; Bohra, M.; Kim, J.-H.; Díaz, R. E.; Vernieres, J.; Grammatikopoulos, P.; Sowwan, M. A Facile Single-Step Synthesis of Ternary Multicore Magneto-Plasmonic Nanoparticles. Nanoscale 2014, 6, 3532−3535.

(10) Sotiriou, G. A. Biomedical Applications of Multifunctional Plasmonic Nanoparticles. Wiley Interdiscip. Rev.: Nanomed. Nanobiotechnol. 2013, 5, 19−30.

(11) Ferrando, R.; Jellinek, J.; Johnston, R. L. Nanoalloys: From Theory to Applications of Alloy Clusters and Nanoparticles. Chem Rev. 2008, 108, 845−910.

(12) Llamosa, D.; Ruano, M.; Martínez, L.; Mayoral, A.; Roman, E.; García-Hernández, M.; Huttel, Y. The Ultimate Step towards a Tailored Engineering of Core-Shell and Core-Shell-Shell Nano-particles. *Nanoscale* **2014**, *6*, 13483–13486.

(13) Sneed, B. T.; Young, A. P.; Jalalpoor, D.; Golden, M. C.; Mao, S.; Jiang, Y.; Wang, Y.; Tsung, C.-K. Shaped Pd-Ni-Pt Core—Sandwich-Shell Nanoparticles: Influence of Ni Sandwich Layers on Catalytic Electrooxidations. *ACS Nano* **2014**, *8*, 7239–7250.

(14) Yang, H.; Bradley, S. J.; Wu, X.; Chan, A.; Waterhouse, G. I. N.; Nann, T.; Zhang, J.; Kruger, P. E.; Ma, S.; Telfer, S. G. General Synthetic Strategy for Libraries of Supported Multicomponent Metal Nanoparticles. *ACS Nano* **2018**, *12*, 4594–4604.

(15) Yu, W.; Porosoff, M. D.; Chen, J. G. Review of Pt-Based Bimetallic Catalysis: From Model Surfaces to Supported Catalysts. *Chem. Rev.* **2012**, *112*, 5780–5817.

(16) Peng, Z.; Yang, H. Designer Platinum Nanoparticles: Control of Shape, Composition in Alloy, Nanostructure and Electrocatalytic Property. *Nano Today* **2009**, *4*, 143–164.

(17) Zhang, L.; Iyyamperumal, R.; Yancey, D. F.; Crooks, R. M.; Henkelman, G. Design of Pt-Shell Nanoparticles with Alloy Cores for the Oxygen Reduction Reaction. *ACS Nano* **2013**, *7*, 9168–9172.

(18) Li, L.; E, Y.; Yuan, J.; Luo, X.; Yang, Y.; Fan, L. Electrosynthesis of Pd/Au Hollow Cone-Like Microstructures for Electrocatalytic Formic Acid Oxidation. *Electrochim. Acta* **2011**, *56*, 6237–6244.

(19) Ahmed, M.; Attard, G. A.; Wright, E.; Sharman, J. Methanol and Formic Acid Electrooxidation on Nafion Modified Pd/Pt{111}: The Role of Anion Specific Adsorption in Electrocatalytic Activity. *Catal. Today* **2013**, *202*, 128–134.

(20) Fan, F.-R.; Liu, D.-Y.; Wu, Y.-F.; Duan, S.; Xie, Z.-X.; Jiang, Z.-Y.; Tian, Z.-Q. Epitaxial Growth of Heterogeneous Metal Nanocrystals: From Gold Nano-Octahedra to Palladium and Silver Nanocubes. *J. Am. Chem. Soc.* **2008**, *130*, 6949–6951.

(21) Sankar, M.; Nowicka, E.; Tiruvalam, R.; He, Q.; Taylor, S. H.; Kiely, C. J.; Bethel, D.; Knight, D. W.; Hutchings, G. J. Controlling the Duality of the Mechanism in Liquid-Phase Oxidation of Benzyl Alcohol Catalysed by Supported Au-Pd Nanoparticles. *Chem. - Eur. J.* **2011**, *17*, 6524–6532.

(22) Zhang, H. X.; Wang, C.; Wang, J.-Y.; Zhai, J.-J.; Cai, W.-B. Carbon-Supported Pd-Pt Nanoalloy with Low Pt Content and Superior Catalysis for Formic Acid Electro-Oxidation. *J. Phys. Chem. C* **2010**, *114*, 6446–6451.

(23) Sasaki, K.; Naohara, H.; Choi, Y. M.; Cai, Y.; Chen, W.-F.; Liu, P.; Adzic, R. R. Highly Stable Pt Monolayer on PdAu Nanoparticle Electrocatalysts for the Oxygen Reduction Reaction. *Nat. Commun.* **2012**, *3*, No. 1115.

(24) Zhang, L.; Henkelman, G. Tuning the Oxygen Reduction Activity of Pd Shell Nanoparticles with Random Alloy Cores. *J. Phys. Chem. C* **2012**, *116*, 20860–20865.

(25) Liu, H. B.; Pal, U.; Medina, A.; Maldonado, C.; Ascencio, J. A. Structural Incoherency and Structure Reversal in Bimetallic Au-Pd Nanoclusters. *Phys. Rev. B* **2005**, *71*, No. 075403.

(26) Paz-Borbón, L. O.; Johnston, R. L.; Barcaro, G.; Fortunelli, A. A Mixed Structural Motif in 34-Atom Pd-Pt Clusters. *J. Phys. Chem. C* **2007**, *111*, 2936–2941.

(27) Tran, D. T.; Johnston, R. L. Study of 40-atom Pt-Au Clusters Using a Combined Empirical Potential-Density Functional Approach. *Proc. R. Soc. A* **2011**, *467*, 2004–2019.

(28) Toshima, N. Capped Bimetallic and Trimetallic Nanoparticles for Catalysis and Information Technology. *Macromol. Symp.* **2008**, *270*, 27–39.

(29) Sharma, G.; Kumar, D.; Kumar, A.; Al-Muhtaseb, A. H.; Pathania, D.; Nausad, M.; Mola, G. T. Revolution from Monometallic to Trimetallic Nanoparticle Composites, Various Synthesis Methods and their Applications: A review. *Mater. Sci. Eng., C* **2017**, *71*, 1216–1230.

(30) Wang, L.; Yamauchi, Y. Autoprogrammed Synthesis of Triple-Layered Au@Pd@Pt Core-Shell Nanoparticles Consisting of a Au@Pd Bimetallic Core and Nanoporous Pt Shell. *J. Am. Chem. Soc.* **2010**, *132*, 13636–13638.

(31) Wang, L.; Yamauchi, Y. Strategic Synthesis of Trimetallic Au@Pd@Pt Core-Shell Nanoparticles from Poly(vinylpyrrolidone)-Based Aqueous Solution toward Highly Active Electrocatalysts. *Chem. Mater.* **2011**, *23*, 2457–2465.

(32) Zhang, X.; Zhang, F.; Chan, K.-Y. Preparation of Pt-Ru-Co Trimetallic Nanoparticles and their Electrocatalytic Properties. *Catal. Commun.* **2004**, *5*, 749–753.

(33) Toshima, N.; Shiraishi, Y.; Matsushita, T.; Mukai, H.; Hirakawa, K. Self-Organization of Metal Nanoparticles and its Application to Syntheses of Pd/Ag/Rh Trimetallic Nanoparticle Catalysts with Triple Core/Shell Structures. *Int. J. Nanosci.* **2002**, *1*, 397–401.

(34) Fang, P.-P.; Duan, S.; Lin, X.-D.; Anema, J. R.; Li, J.-F.; Buriez, O.; Ding, Y.; Fan, F.-R.; Wu, D.-Y.; Ren, B.; Wang, Z. L.; Amatore, C.; Tian, Z.-Q. Tailoring Au-Core Pd-Shell Pt-Cluster Nanoparticles for Enhanced Electrocatalytic Activity. *Chem. Sci.* **2011**, *2*, 531–539.

(35) Kang, S. W.; Lee, Y. W.; Park, Y.; Choi, B.-S.; Hong, J. W.; Park, K.-H.; Han, S. W. One-Pot Synthesis of Trimetallic Au@PdPt Core-Shell Nanoparticles with High Catalytic Performance. *ACS Nano* **2013**, *7*, 7945–7955.

(36) Kondrat, S. A.; Miedziak, P. J.; Douthwaite, M.; Brett, G. L.; Davies, T. E.; Morgan, D. J.; Edwards, J. K.; Knight, D. W.; Kiely, C. J.; Taylor, S. H.; Hutchings, G. J. Base-Free Oxidation of Glycerol Using Titania-Supported Trimetallic Au-Pd-Pt Nanoparticles. *ChemSusChem* **2014**, *7*, 1326–1334.

(37) He, Q.; Miedziak, P. J.; Kesavan, L.; Dimitratos, N.; Sankar, M.; Lopez-Sanchez, J. A.; Forde, M. M.; Edwards, J. K.; Knight, D. W.; Taylor, S. H.; Kiely, C. J.; Hutchings, G. J. Switching-Off Toluene Formation in the Solvent-Free Oxidation of Benzyl Alcohol Using Supported Trimetallic Au-Pd-Pt Nanoparticles. *Faraday Discuss.* **2013**, *162*, 365–378.

(38) Metzler, M.; Thorwart, A.; Zeller, S.; Diemant, T.; Behm, R. J.; Jacob, T. Electroless Deposition of Au/Pt/Pd Nanoparticles on *p*-Si(111) for the Light-Induced Hydrogen Evolution Reaction. *Catal. Today* **2015**, *244*, 3–9.

(39) Zhang, G.-R.; Wu, J.; Xu, B.-Q. Syntheses of Sub-30 nm Au@Pd Concave Nanocubes and Pt-on-(Au@Pd) Trimetallic Nanostructures as Highly Efficient Catalysts for Ethanol Oxidation. *J. Phys. Chem. C* **2012**, *116*, 20839–20847.

(40) Huang, L.; Han, Y.; Dong, S. Highly-Branched Mesoporous Au-Pd-Pt Trimetallic Nanoflowers Blooming on Reduced Graphene Oxide as an Oxygen Reduction Electrocatalyst. *Chem. Commun.* **2016**, *52*, 8659–8662.

(41) Cai, X.-L.; Liu, C.-H.; Liu, J.; Lu, Y.; Zhong, Y.-N.; Nie, K.-Q.; Xu, J.-L.; Gao, X.; Sun, X.-H.; Wang, S.-D. Synergistic Effects in CNTs-PdAu/Pt Trimetallic Nanoparticles with High Electrocatalytic Activity and Stability. *Nano-Micro Lett.* **2017**, *9*, 48 (10pp). .

(42) Zhang, H.; Lu, L.; Cao, Y.; Du, S.; Cheng, Z.; Zhang, S. Fabrication of Catalytically Active Au/Pt/Pd Trimetallic Nanoparticles by Rapid Injection of NaPBH₄. *Mater. Res. Bull.* **2014**, *49*, 393–398.

(43) Hutchings, G. J. Selective Oxidation Using Supported Gold Bimetallic and Trimetallic Nanoparticles. *Catal. Today* **2014**, *238*, 69–73.

(44) Chanmanee, W.; De Tacconi, N. R.; Rajeshwar, K.; Lin, W.-Y.; Nikiel, L.; Wampler, W. A. Photocatalytically Generated Trimetallic (Pt-Pd-Au/C-TiO₂) Nanocomposite Electrocatalyst. *J. Electrochem. Soc.* **2012**, *159*, F226–F233.

(45) Fan, T.-E.; Liu, T.-D.; Zheng, J.-W.; Shao, G.-F.; Wen, Y.-H. Structural Optimization of Pt-Pd-Au Trimetallic Nanoparticles by Discrete Particle Swarm Algorithms. *J. Mater. Sci.* **2015**, *50*, 3308–3319.

(46) Wu, G.-H.; Liu, Q.-M.; Wu, X. Geometrical and Energetic Properties in 38-Atom Trimetallic Au-Pd-Pt Clusters. *Chem. Phys. Lett.* **2015**, *620*, 92–97.

(47) Zhao, Z.; Li, M.; Cheng, D.; Zhu, J. Understanding the Structural Properties and Thermal Stabilities of Au-Pd-Pt Trimetallic Clusters. *Chem. Phys.* **2014**, *441*, 152–158.

(48) Wu, X.; Dong, Y. Theoretical Studies of Structures and Energies of Pd, Au-Pd, and Au-Pd-Pt Clusters. *New J. Chem.* **2014**, *38*, 4893–4900.

(49) Grammatikopoulos, P.; Steinhauer, S.; Vernieres, J.; Singh, V.; Sowwan, M. Nanoparticle Design by Gas-Phase Synthesis. *Adv. Phys.: X* **2016**, *1*, 81–100.

(50) Crist, B. V. Au⁰. In *Handbook of Monochromatic XPS Spectra: The Elements and Native Oxides*; John Wiley and Sons: Chichester, U.K., 2000; pp 17–21.

(51) Crist, B. V. Pt⁰. In *Handbook of Monochromatic XPS Spectra: The Elements and Native Oxides*; John Wiley and Sons: Chichester, U.K., 2000; pp 212–215.

(52) Crist, B. V. Pd⁰. In *Handbook of Monochromatic XPS Spectra: The Elements and Native Oxides*; John Wiley and Sons: Chichester, U.K., 2000; pp 204–207.

(53) (a) Foiles, S. M.; Baskes, M. I.; Daw, M. S. Embedded-Atom-Method Functions for the FCC Metals Cu, Ag, Au, Ni, Pd, Pt, and their Alloys. *Phys. Rev. B* **1986**, *33*, 7983–7991;(b) Camley, R. E.; Mills, D. L. Erratum: Collective excitations of semi-infinite super-lattice structures: Surface plasmons, bulk plasmons, and the electron-energy-loss spectrum. *Phys. Rev. B* **1988**, *37*, No. 10378.

(54) Rakhtsaum, G. Platinum Alloys: A Selective Review of the Available Literature. *Platinum Met. Rev.* **2013**, *57*, 202–213.

(55) Ma, Y.; Balbuena, P. B. Pt Surface Segregation in Bimetallic Pt₃M Alloys: A Density Functional Theory Study. *Surf. Sci.* **2008**, *602*, 107–113.

(56) Mallát, T.; Petró, J. The Activity and Surface Composition of Platinum-Gold Catalysts. *Appl. Catal.* **1982**, *4*, 257–265.

(57) Shan, B.; Wang, L.; Yang, S.; Hyun, J.; Kapur, N.; Zhao, Y.; Nicholas, J. B.; Cho, K. First-Principles-Based Embedded Atom Method for PdAu Nanoparticles. *Phys. Rev. B* **2009**, *80*, No. 035404.

(58) Barcaro, G.; Fortunelli, A.; Polak, M.; Rubinovich, L. Patchy Multishell Segregation in Pd-Pt Alloy Nanoparticles. *Nano Lett.* **2011**, *11*, 1766–1769.

(59) Adams, J. B.; Foiles, S. M.; Wolfer, W. G. Self-Diffusion and Impurity Diffusion of FCC Metals Using the Five-Frequency Model and the Embedded Atom Method. *J. Mater. Res.* **1989**, *4*, 102–112.

(60) Kittel, C. *Introduction to Solid State Physics*, 6th ed.; Wiley: New York, 1986.

(61) Ziegler, J. F.; Biersack, J. P.; Littmark, U. *The Stopping and Range of Ions in Matter*; Pergamon: New York, 1985.

(62) Nordlund, K. *PARCAS Computer Code*; Purdue University: West Lafayette, IN, 2006.

(63) Nordlund, K.; Ghaly, M.; Averback, R. S.; Caturla, M.; Diaz de la Rubia, T.; Tarus, J. Defect Production in Collision Cascades in Elemental Semiconductors and FCC Metals. *Phys. Rev. B* **1998**, *57*, 7556 (15pp). .

(64) Ghaly, M.; Nordlund, K.; Averback, R. S. Molecular Dynamics Investigations of Surface Damage Produced by Kiloelectronvolt Self-Bombardment of Solids. *Philos. Mag. A* **1999**, *79*, 795–820.

(65) Berendsen, H. J. C.; Postma, J. P. M.; van Gunsteren, W. F.; DiNola, A.; Haak, J. R. Molecular Dynamics with Coupling to an External Bath. *J. Chem. Phys.* **1984**, *81*, 3684–3690.

(66) Bohra, M.; Grammatikopoulos, P.; Singh, V.; Zhao, J.; Toulkeridou, E.; Steinhauer, S.; Kioseoglou, J.; Bobo, J.-F.; Nordlund, K.; Djurabekova, F.; Sowwan, M. Tuning the Onset of Ferromagnetism in Heterogeneous Bimetallic Nanoparticles by Gas Phase Doping. *Phys. Rev. Mater.* **2017**, *1*, No. 066001.

(67) Plimpton, S. J. Fast Parallel Algorithms for Short-Range Molecular Dynamics. *J. Comput. Phys.* **1995**, *117*, 1–19.

(68) Nosé, S. A Unified Formulation of the Constant Temperature Molecular Dynamics Methods. *J. Chem. Phys.* **1984**, *81*, 511–519.

(69) Hoover, W. G. Canonical Dynamics: Equilibrium Phase-Space Distributions. *Phys. Rev. A* **1985**, *31*, 1695–1697.

(70) Hestenes, M. R.; Stiefel, E. Methods of Conjugate Gradients for Solving Linear Systems. *J. Res. Natl. Bur. Stand.* **1952**, *49*, 409–436.

(71) Wales, D. J.; Doye, J. P. K. Global Optimization by Basin-Hopping and the Lowest Energy Structures of Lennard-Jones Clusters Containing up to 110 Atoms. *J. Phys. Chem. A* **1997**, *101*, 5111–5116.

(72) Wales, D. J.; Scheraga, H. A. Global Optimization of Clusters, Crystals, and Biomolecules. *Science* **1999**, *285*, 1368–1372.

(73) Stukowski, A. Visualization and Analysis of Atomistic Simulation Data with OVITO—the Open Visualization Tool. *Modell. Simul. Mater. Sci. Eng.* **2010**, *18*, No. 015012.

(74) Grammatikopoulos, P.; Kioseoglou, J.; Galea, A.; Vernieres, J.; Benelmekki, M.; Diaz, R. E.; Sowwan, M. Kinetic Trapping through Coalescence and the Formation of Patterned Ag-Cu Nanoparticles. *Nanoscale* **2016**, *8*, 9780–9790.

(75) Vernieres, J.; Benelmekki, M.; Kim, J.-H.; Grammatikopoulos, P.; Bobo, J.-F.; Diaz, R. E.; Sowwan, M. Single-Step Gas Phase Synthesis of Iron Aluminide Nanoparticles with Soft Magnetic Properties. *APL Mater.* **2014**, *2*, No. 116105.

(76) Singh, V.; Cassidy, C.; Pedersen, F. A.; Kim, J.-H.; Aranishi, K.; Kumar, S.; Lal, C.; Gspan, C.; Grogger, W.; Sowwan, M. Engineering High-Performance Pd Core-MgO Porous Shell Nanocatalysts via Heterogeneous Gas-Phase Synthesis. *Nanoscale* **2015**, *7*, 13387–13392.

(77) Benelmekki, M.; Vernieres, J.; Kim, J.-H.; Diaz, R. E.; Grammatikopoulos, P.; Sowwan, M. On the Formation of Ternary Metallic-Dielectric Multicore-Shell Nanoparticles. *Mater. Chem. Phys.* **2015**, *151*, 275–281.

(78) A Simple Sputter Yield Calculator. https://www.iap.tuwien.ac.at/www/surface/sputteryield (accessed Jan 11, 2019).

(79) Matsunami, N.; Yamamura, Y.; Itikawa, Y.; Itoh, N.; Kazumata, Y.; Miyagawa, S.; Morita, K.; Shimizu, R.; Tawara, H. Energy Dependence of the Ion-Induced Sputtering Yields of Monatomic Solids. *At. Data Nucl. Data Tables* **1984**, *31*, 1–80.

(80) Vernieres, J.; Steinhauer, S.; Zhao, J.; Chapelle, A.; Menini, P.; Dufour, N.; Diaz, R. E.; Nordlund, K.; Djurabekova, F.; Grammatikopoulos, P.; Sowwan, M. Gas Phase Synthesis of Multifunctional Fe-Based Nanocubes. *Adv. Funct. Mater.* **2017**, *27*, No. 1605328.

(81) Grammatikopoulos, P.; Sowwan, M. Nanoparticle Formation via Magnetron Sputtering with Inert Gas Aggregation. In *Nano-structured Semiconductors: Amorphisation and Thermal Properties*; Termentzidis, K., Ed.; Pan Stanford Publishing: New York, 2017; pp 436–443.

(82) Zanti, G.; Peeters, D. Electronic Structure Analysis of Small Gold Clusters Auₘ (m ≤ 16) by Density Functional Theory. *Theor. Chem. Acc.* **2013**, *132*, No. 1300.

(83) Zanti, G.; Peeters, D. DFT Study of Bimetallic Palladium-Gold Clusters PdₙAuₘ of Low Nuclearities (n + m ≤ 14). *J. Phys. Chem. A* **2010**, *114*, 10345–10356.

(84) Jain, P. K. A DFT-Based Study of the Low-Energy Electronic Structures and Properties of Small Gold Clusters. *Struct. Chem.* **2005**, *16*, 421–426.

(85) Ferrari, P.; Hussein, H. A.; Heard, C. J.; Vanbuel, J.; Johnston, R. L.; Lievens, P.; Janssens, E. Effect of Palladium Doping on the Stability and Fragmentation Patterns of Cationic Gold Clusters. *Phys. Rev. A* **2018**, *97*, No. 052508.

(86) Winczewski, S.; Rybicki, J. Structure of Small Platinum Clusters Revised. *Comput. Methods Sci. Technol.* **2011**, *17*, 75–85.

(87) Xiao, L.; Wang, L. Structures of Platinum Clusters: Planar or Spherical? *J. Phys. Chem. A* **2004**, *108*, 8605–8614.

(88) Li, J.; Zhai, H.-J.; Wang, L.-S. Au₂₀: A Tetrahedral Cluster. *Science* **2003**, *299*, 864–867.

(89) Ferrando, R. *Structure and Properties of Nanoalloys*; Elsevier: Amsterdam, 2016; pp 22–28.

(90) Ling, T.; Xie, L.; Zhu, J.; Yu, H.; Ye, H.; Yu, R.; Cheng, Z.; Liu, L.; Liu, L.; Yang, G.; Cheng, Z.; Wang, Y.; Ma, X. Icosahedral Face-Centered Cubic Fe Nanoparticles: Facile Synthesis and Character-ization with Aberration-Corrected TEM. *Nano Lett.* **2009**, *9*, 1572–1576.

(91) Nellist, P. D.; Pennycook, S. J. The Principles and Interpretation of Annular Dark-Field Z-Contrast Imaging. *Adv. Imaging Electron Phys.* **2000**, *113*, 147–203.

(92) Strein, T. G.; Ewing, A. G. Characterization of Small Noble Metal Microelectrodes by Voltammetry and Energy-Dispersive X-ray Analysis. *Anal. Chem.* **1993**, *65*, 1203−1209.